

Development of miniature bar-type structural fuses with cold formed bolted connections

Dongzhi Guan^{1,2a}, Sen Yang^{1b}, Liang-Jiu Jia^{*3} and Zhengxing Guo^{1,2c}

¹School of Civil Engineering, Southeast University, Nanjing 211189, China

²Key Laboratory of Concrete and Pre-Stressed Concrete Structures of the Ministry of Education, Nanjing 211189, China

³Department of Disaster Mitigation for Structures, Tongji University, Shanghai 200092, China

(Received January 24, 2019, Revised December 2, 2019, Accepted December 8, 2019)

Abstract. A novel all-steel miniature bar-type structural fuse (MBSF) with cold formed bolted connections is developed in this study, which consists of a central energy dissipation core cut from a smooth round bar, an external confining tube and nuts. Three types of cross sections for the central energy dissipation core, i.e., triple-cut, double-cut and single-cut cross sections, were studied. Totally 18 specimens were axially tested under either symmetric or asymmetric cyclic loading histories, where the parameters such as cut cross sectional area ratio, length of the yielding portion and cross sectional type were investigated. Numerical simulation of 2 representative specimens were also conducted. An analytical model to evaluate the bending failure at the elastic portion was proposed, and a design method to avoid this failure mode was also presented. The experimental results show that the proposed MBSFs exhibit satisfactory hysteretic performance under both the two cyclic loading histories. Average strain values of 8% and 4% are found to be respectively suitable for designing the new MBSFs as the ultimate strain under the symmetric and asymmetric cyclic loadings.

Keywords: structural fuses; quasi-triangular cross section; seismic performance; cyclic loading; steel

1. Introduction

Prefabricated buildings, including steel and concrete structures, are being increasingly applied around the world for the merits such as better-quality control, higher construction speed and less site labor (Guan *et al.* 2016, Gorgun 2018). Besides, prefabricated structures are also regarded as an inevitable choice in terms of sustainability for buildings, which focuses on resources use and environmental effects (Fleischman and Seeber 2016). The earthquake-resistant concept of prefabricated structures can be illustrated in the two seismic design philosophies, i.e., “emulative” and “jointed” systems (Ghosh *et al.* 1997). The precast emulative systems, widely employed in practice, are intended to achieve similar seismic performance as conventional site-made structures (Guan *et al.* 2018). The damage to the load-bearing elements in this system, especially in plastic hinge zones, leads to extensive repair costs, business downtime, or even demolition of the emulative precast structures. Beyond the emulative ones,

the precast jointed systems are developed to achieve satisfactory seismic performance without considerable damage to the precast units, which are related to damage avoidance design method. A more recent practice is to employ ductile seismic structural fuses to dissipate dynamic response energy in the precast jointed systems. The fuses become the key point to protect the structures from earthquake attacks with low costs. Among different types of structural fuses (Wada *et al.* 2000, Morgen and Kurama 2007, Calado *et al.* 2013, Nikoukalam and Dolatshahi 2015), axially yielding energy dissipation fuses are one of the most promising devices owing to their merits, e.g., wide applicability, low cost, stable properties and easy construction, etc.

As the increasing acceptance of buckling-restrained mechanism (Zhou *et al.* 2014), several miniature replaceable buckling-restrained energy dissipation fuses were developed. Christopoulos *et al.* (2002) inserted energy dissipation bars in steel confining cylinders to limit buckling. Test results showed that permanent deformation of the threaded portion resulted in a flat force-displacement response when the load turned from tension to compression. Oktavianus *et al.* (2019) investigated an innovative replaceable buckling-restrained fuse (RBRF) applied at steel beam ends. Pampanin (2005) introduced a replaceable buckling-restrained fuse-type mild steel energy dissipater, consisting of a deformed bar machined down and inserted in a grouted metallic cylinder. A number of quasi-static experiments were conducted on the fuse-type energy dissipaters under positive cyclic loadings (termed as asymmetric cyclic loading in this study) or cyclic loadings

*Corresponding author, Associate Professor
E-mail: lj_jia@tongji.edu.cn

^a Lecturer
E-mail: guandongzhi@seu.edu.cn

^b Ph.D Candidate
E-mail: 463510751@qq.com

^c Professor
E-mail: guozx195608@126.com

in positive and negative directions alternately (termed as symmetric cyclic loading) (Marriott *et al.* 2009, Amaris Mesa 2010, Sarti *et al.* 2013). This energy dissipater with a slenderness ratio of 60 behaved with stable hysteresis loops under the asymmetric cyclic loading. However, contact between the infilled material and the transition zones of the bar in the energy dissipater caused significantly increased stiffness when the dissipater was subjected to the symmetric cyclic loading. White (2014) developed so-called “dry” buckling-restrained fuse-type energy dissipaters, which had no infilling materials such as epoxy or grout between the energy dissipation bars and confining tubes. Cyclic tension-compression loading tests showed that the groove type energy dissipater exhibited good behaviors, but the sharp cross sectional profile might lead to susceptibility to low-cycle fatigue failure.

It can be concluded that buckling-restrained axially yielding energy dissipaters with grout infilled have high possibilities to fail prematurely due to failure of the infilling materials such as epoxy and mortar. In addition, the configurations and fabrication details also affect seismic performance of small axially yielding energy dissipaters significantly. This paper contributes to developing a new form of all-steel miniature bar-type structural fuse (MBSFs) without infilling materials, which can be easily manufactured and installed. The 2 ends of the newly proposed MBSFs are bolted to adjacent structural components, where standardized threads were manufactured at the 2 ends by a straightforward thread rolling process. This leads to great ease and low costs of the newly proposed MBSFs, since no complicated manufacturing is required to make the threads. Experimental study of 18 MBSF specimens was conducted under both asymmetric and symmetric cyclic loading histories. The failure modes and corresponding mechanism were investigated through the experiments. In addition, numerical simulations were also conducted to investigate the buckling modes and failure mechanism of 2 representative specimens. Finally, design suggestions of the newly proposed MBSFs was presented.

2. Experimental program

MBSFs have a great potential to be applied to many structures, especially precast steel or concrete frame structures for the purpose of damage mitigation. Fig. 1 shows 2 typical precast steel and concrete beam-column connections, i.e., gap-opening system and top-connecting system (Christopoulos *et al.* 2002, Mander *et al.* 2009, Amaris Mesa 2010). In Fig. 1(a), when the gap between the beam and the column opens under earthquake loadings, the MBSF is under tension leading to elongation of the energy dissipation core. However, compression between the beam and the column is transferred by direct interaction of the steel or concrete components, the MBSF has little or no compressive deformation compared with the original configurations. In Fig. 1(b), the steel or precast concrete beam is supported by the top hinge and connected to the column by post-tensioned strands. Because the top hinge

acts as a pivot point under earthquake loadings, the core of the bottom MBSF is elongated and shortened alternatively reducing the peak seismic response of the main structure and dissipating energy induced by earthquakes. Therefore, stable hysteretic behaviors of the newly proposed MBSFs are required under both tension and compression. Previous investigations indicate that premature cracking of the infilling material impairs the hysteretic performance of the MBSFs within the compressive reversals, which leads to difficulties in applying the MBSFs to the case illustrated in Fig. 1(b). Therefore, it is more suitable to design and manufacture the new all-steel MBSFs.

Owing to the relatively small sizes of the MBSFs, a great number of MBSFs are necessary for the seismic protection of a conventional building. Aimed at massive application, it is important for MBSFs to be manufactured easily with low costs. For massive production, MBSFs also have to be robust with respect to manufacturing deviations. Fig. 2 gives the configuration and details of the newly proposed MBSF schematically. The MBSF consists of 3 main components: (a) a central energy dissipation core; (b) a confining tube; (c) several nuts. The central energy dissipation core, made of a conventional mild steel bar, can be divided into several parts illustrated in Fig. 2, i.e., the yielding portion, transition portion, elastic portion and the thread portion. The yielding portion is manufactured by the wire-electrode cutting or mechanical cold forming process. The cross section of the yielding portion is made into a quasi-triangular shape with some small remaining arcs of the original circular section. The remaining arcs are intended to contact with the external confining tube, preventing excessive buckling deformation of the yielding portion. The 2 ends of the central energy dissipation core are machined into standardized threads by a thread rolling process. The thread portions of the core are not weaker than the other portions because some steel is rolled and squeezed into the original bar in the range of threads. This cold forming process can greatly increase the elastic limit of the thread portions (Huang 2016, Xing 2004). The elastic portions remain the initial shape of the bar. For the design, the elastic portions are expected to be elastic before the ultimate strength of the yielding portion is achieved for the MBSF. One of the elastic portions is long enough to guarantee the restraining length for the central core under large tensile loading displacements. This design is of great importance to avoid premature buckling at the transition portions or the elastic portions. Seamless steel tubes, which are cheap and easy to obtain, are employed as the confining tubes. The diameter of the central core is 1-2 mm smaller than the inner diameter of the confining tube, leading to a small gap between the internal core and the external restraining tube. Lubricating oil is also utilized to reduce the potential friction between the core and the tube. Standard nuts are screwed on the thread portions of the core to connect the newly proposed MBSF with main structures. The nut close to the short elastic portion can be connected to the confining tube by spot-welding in practice, which is considered a stopper to avoid the relative longitudinal rigid movement between the confining tube and the central core.

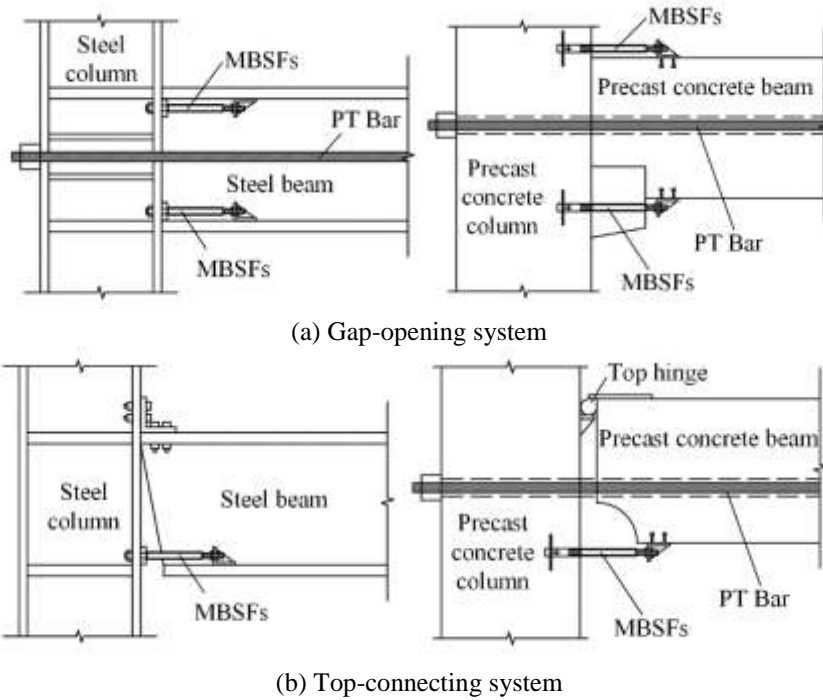


Fig. 1 Applications of MBSFs in precast hybrid beam-column connections

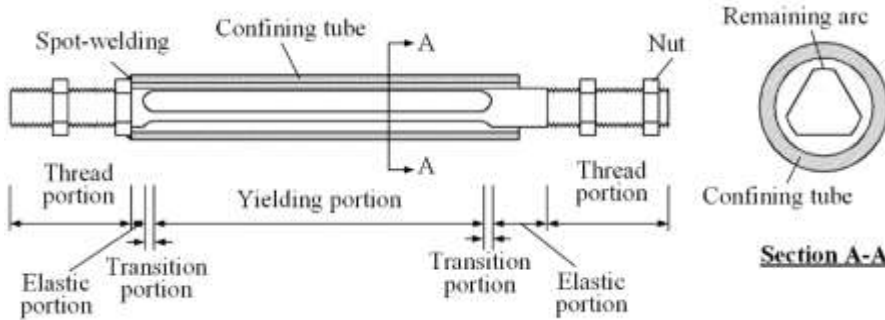


Fig. 2 Details of MBSFs

3. Research program

Totally 18 MBSF specimens were designed and manufactured to study the effects of the loading history, length of the yielding portion, the cross sectional shape, and cut cross sectional area ratio defined as follows

$$R_a = \frac{A_c}{A_0} \quad (1)$$

where R_a is the cut cross sectional area ratio, A_c is the cross sectional area of the removed portion, A_0 is the cross sectional area of the raw bars. A series of cyclic loading tests were carried out to investigate seismic performance and failure modes of the newly proposed MBSFs.

3.1 Description of specimens

In this study, the first specimen was designed, assuming to be employed in a gap-opening beam-column connection with a beam height of 400 mm, and the prototype structure was designed to achieve the collapse prevention (CP) performance level (4% storey drift angle) (ASCE41-06 2007). A simplified gap-opening mechanism was utilized to design the first specimen, and other specimens were designed based on the first specimen. The basic design parameters are illustrated in Fig. 3. All the central energy dissipation cores were manufactured using conventional steel round bars with a diameter of 20 mm. The transition portion, connecting the yielding portion and the elastic portion, was made into smooth arcs with a radius of 10 mm to avoid strain concentration in this area. The length of the thread portion was designed as 160 mm, which was long enough to install the specimen into the test setup with

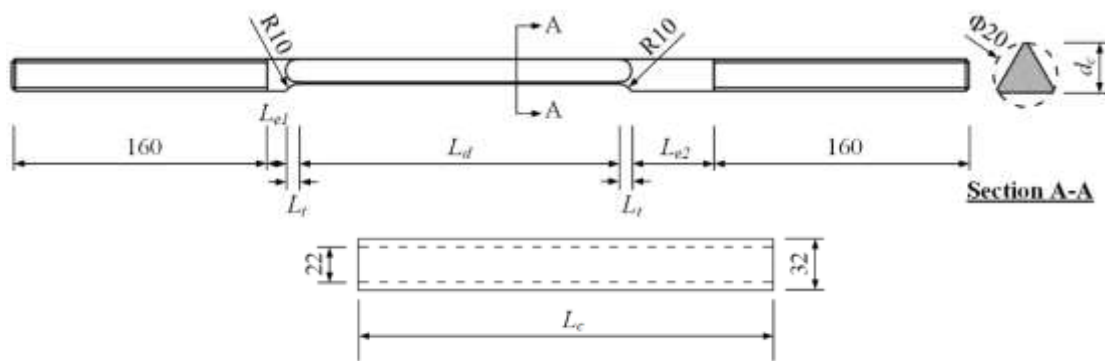


Fig. 3 Geometrical parameters of MBSF specimens Notes: L_{e1} , L_{e2} = length of elastic portions, L_t =length of transition portions, L_d =length of yielding portions, L_c =length of confining tubes, d_c =sectional height of yielding portions



Fig. 4 Wire-electrode cutting process of specimens

standard nuts. For manufacturing of the central energy dissipation core, raw round steel bars were cut into the designed length firstly. Then standard threads were manufactured by a thread rolling machine using a cold forming process. This process made the elastic limit of the thread portions higher than the other parts of the core. Because the raw steel bars with a diameter of 20 mm were not stiff enough to resist machining deformations triggered by the mechanical cold forming process, a wire-electrode cutting process was utilized to manufacture the transition portions and the yielding portion smoothly and fast, as shown in Fig. 4. As to stiffer raw steel bars with larger diameters, a cold working machine can be employed to manufacture the yielding portions to further reduce the cost.

To investigate the required strength of the elastic portion to avoid premature buckling at the ends, 4 different cross sectional areas of the yielding portions were determined as 155, 203, 246 and 282 mm², corresponding to an R_a value of 50.7%, 35.4%, 21.7%, 10.2%, respectively. Length of the yielding portions of the specimens was 200, 166, 133 and 100 mm, respectively. The quasi-triangular cross section of

the yielding portion required triple-cut of the raw bar, 2 additional cross sectional shapes for the yielding portions, as shown in Fig. 5, were also designed to reduce the cutting times and also the manufacturing cost. The single-cut cross section shown in Fig. 5(a) was cut only once, and the specimens had inherent initial eccentricity due to the unsymmetrical cutting. The double-cut cross section was cut twice, which was symmetrical with 2 axes of the cross section.

The parameters of the tested specimens are presented in Table 1. For the nomenclature of the specimens, the first character represented the cross sectional shape of the yielding portion, where “T”, “D” and “S” corresponded to the triple-cut, double-cut and single-cut cross section, respectively. The number after the character “C” indicated the approximate integer of R_a multiplying by 100. The length of the yielding portions was expressed in centimeter as the number after the character “L”. The last character represented the loading history, where “A” indicated asymmetric cyclic loading and “S” the symmetric one.

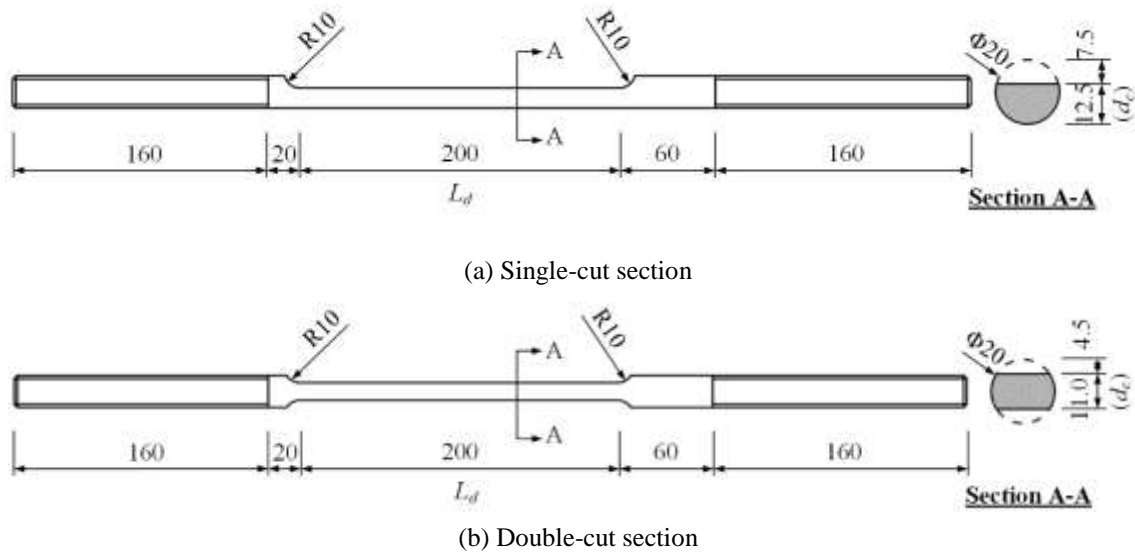


Fig. 5 Specimen details of different section types Note: L_d and d_c denotes length of yielding portions and sectional height of yielding portions, respectively.

Table 1 Design parameters of test specimens

No.	Specimen	L_d	L_t	L_{e1}	L_{e2}	d_c	Areas of yielding portion (mm ²)	Loading history
1	TC50L20-A	200	8.35	11.65	51.65	15.5	155	asymmetric
2	TC50L20-S	200	8.35	11.65	51.65	15.5	155	symmetric
3	TC35L20-A	200	7.6	12.4	52.4	16.5	203	asymmetric
4	TC35L20-S	200	7.6	12.4	52.4	16.5	203	symmetric
5	TC20L20-A	200	6.61	13.39	53.39	17.5	246	asymmetric
6	TC20L20-S	200	6.61	13.39	53.39	17.5	246	symmetric
7	TC10L20-A	200	5.27	14.73	54.73	18.5	282	asymmetric
8	TC10L20-S	200	5.27	14.73	54.73	18.5	282	symmetric
9	TC50L16-A	166	8.35	11.65	51.65	15.5	155	asymmetric
10	TC50L16-S	166	8.35	11.65	51.65	15.5	155	symmetric
11	TC50L13-A	133	8.35	11.65	51.65	15.5	155	asymmetric
12	TC50L13-S	133	8.35	11.65	51.65	15.5	155	symmetric
13	TC50L10-A	100	8.35	11.65	51.65	15.5	155	asymmetric
14	TC50L10-S	100	8.35	11.65	51.65	15.5	155	symmetric
15	DC35L20-A	200	8.35	11.65	51.65	11.0	208	asymmetric
16	DC35L20-S	200	8.35	11.65	51.65	11.0	208	symmetric
17	SC35L20-A	200	9.68	10.32	50.32	12.5	207	asymmetric
18	SC35L20-S	200	9.68	10.32	50.32	12.5	207	symmetric

Notes: L_{e1} , L_{e2} = length of elastic portions, L_t = length of transition portions, L_d = length of yielding portions, L_c = length of confining tubes, d_c = sectional height of yielding portions

Table 2 Geometric dimensions of central cores (Unit: mm)

No.	Specimens	L_d	d_c			d_0	
			Movable end	Center	Fixed end	Long elastic portion	Short elastic portion
1	TC50L20-A	201.0	14.44	14.38	14.79	19.73	19.26
2	TC50L20-S	201.8	15.27	14.95	15.27	20.14	20.18
3	TC35L20-A	202.0	15.71	15.61	15.88	19.53	19.17
4	TC35L20-S	201.3	15.28	15.39	15.36	19.21	19.01
5	TC20L20-A	201.3	16.64	16.78	17.13	19.46	19.67
6	TC20L20-S	202.1	16.63	17.51	16.63	19.57	19.7
7	TC10L20-A	202.9	17.57	17.05	17.57	19.54	19.64
8	TC10L20-S	200.7	17.51	17.67	17.95	19.54	19.39
9	TC50L16-A	165.5	14.94	14.97	15.21	18.82	18.85
10	TC50L16-S	167.2	15.09	15.14	15.33	19.69	19.4
11	TC50L13-A	133.0	14.93	15.01	15.16	19.75	19.52
12	TC50L13-S	134.2	14.65	14.90	15.09	19.48	19.62
13	TC50L10-A	103.5	14.80	14.81	14.87	19.41	19.29
14	TC50L10-S	101.8	14.81	14.97	15.09	19.67	19.27
15	DC35L20-A	202.0	10.86	10.82	10.96	20.24	20.15
16	DC35L20-S	202.8	11.16	11.14	11.22	20.26	20.23
17	SC35L20-A	204.0	11.40	11.94	12.30	20.11	20.58
18	SC35L20-S	203.0	11.70	11.96	12.44	20.2	20.21

Note: d_0 = diameter of elastic portions

Table 3 Material properties

Component	Young's modulus (GPa)	Yielding strength (MPa)	Tensile strength (MPa)	Elongation (%)
Energy dissipation core	218.9	268.4	420.7	39.8
Confining tube	202.6	346.7	503.4	40.6

Due to large relative deformation between the internal energy dissipation core and the external confining tube at the movable end of the MBSF, a longer elastic portion (L_{e2}) was designed to avoid premature failure at the transition portion. Thus, all the confining tubes were made with a length of $(1/2L_{e2}+L_{e1}+2L_t+L_d)$ according to the central cores, as illustrated in Fig. 3. The gap between the energy dissipation core and the confining tube was designed to be 1 mm at each side, and the thickness of the confining tubes was 5 mm to make the tubes remain elastic during the testing. The effect of the confining tube thickness will be investigated in another study. Because the test setup in this experimental investigation was mounted in a vertical position as shown in Fig. 6, the confining tubes were mounted directly onto the nuts without spot-welding to simplify the manufacturing process of the specimens.

In this study, the actual dimensions of the yielding portions were measured and listed in Table 2. The variables L_d and d_c are the averages of the measured dimensions at each cutting side of the specimens. The cross sectional height of the yielding portions near the movable end, the

center of the yielding portions and the fixed end are provided in Table 2, respectively.

3.2 Material properties

The raw steel round bars, made of Chinese low carbon structural steel grade Q235 with a nominal yield strength of 235 MPa, were employed to manufacture the central energy dissipation cores. The confining tubes were made of conventional seamless steel tubes of Q345 with a nominal yield strength of 345 MPa. Coupon tests of the steel bars and the seamless steel tubes were conducted to obtain the actual material properties. The test results are given in Table 3.

3.3 Test setup

Though there are small moments at the ends of the MBSF in the beam-column connections, this effect is not considered in the test setup shown in Fig. 6, which can be studied in future studies on the beam-column connections.

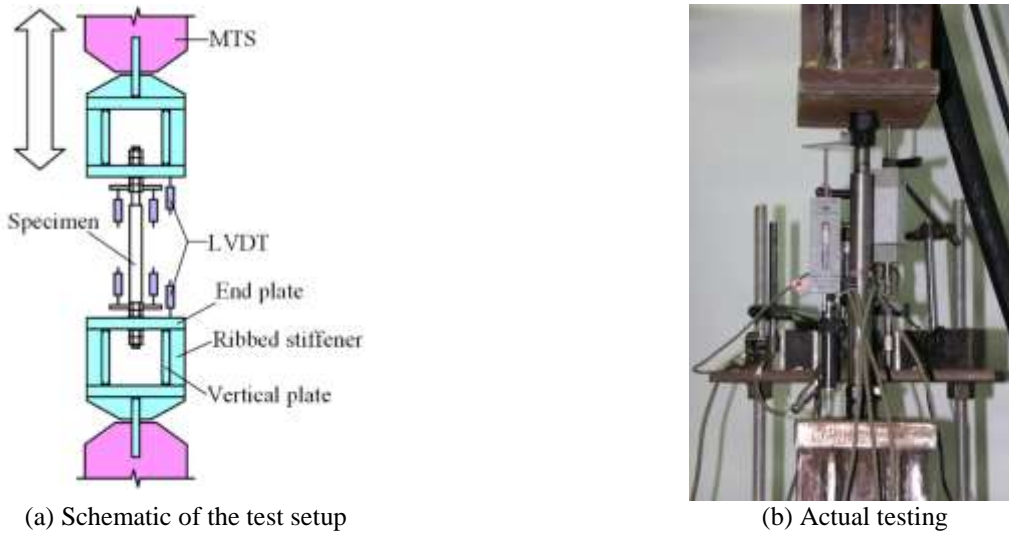


Fig. 6 Test setup

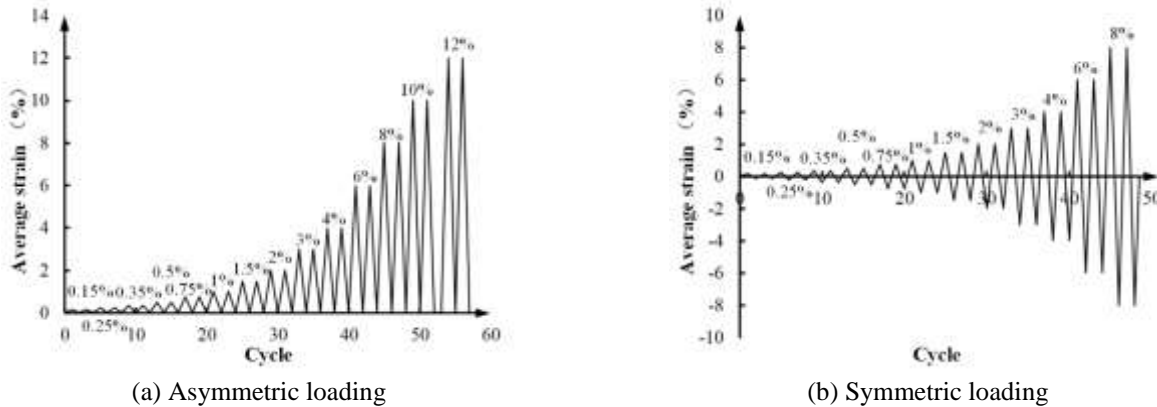


Fig. 7 Loading protocols

The specimens were mounted into an MTS electro-hydraulic testing system with a load capacity of 250 kN. Two stiff bearings were manufactured and clamped by the loading heads of the testing system. The connections between the bearings and the MBSF specimens were similar to those illustrated in Fig. 1, which was also aimed to achieve the boundary conditions similar to those in an actual beam-column connection. The top loading head was movable, and the bottom one fixed. Enforced cyclic displacement loading was applied to the tested specimens by the movable end. The end plate of the bearings was 30 mm thick, and ribbed stiffeners were welded to the vertical plates and the end plate to make the bearing stiff enough. Four nuts were utilized to connect the MBSF specimen with the end plate at each side.

Six linear variable differential transformers (LVDTs) were employed to measure the displacements of the specimens and the bearings. The measuring points of the end plates were located as close to the specimen as possible to reduce the influence of the minor elastic deformation of the end plates. The applied forces were obtained from the load cell of the testing system.

3.4 Loading history

As mentioned in the previous section, the newly proposed MBSFs are mainly subjected to tensile deformation with minor or no compressive one if they are used in the gap-opening system. When installed in the top-connecting system, the MBSFs will be subjected to both tensile and compressive deformation. Therefore, in this test program, the MBSF specimens were tested under both asymmetric and symmetric cyclic loadings as illustrated in Fig. 7. There were 2 tested specimens for each configuration, with one tested under the former loading history and the other one under the latter.

The loading history was determined according to the cyclic loading conditions where the MBSFs were installed. In this study, the MBSFs were expected to be employed in a steel or precast concrete beam-column connection prototype with a beam depth of 400 mm. The controlling displacement for the tests was computed based on the deformation of the yielding portion assuming that the other portions remained elastic. Thus, the controlling displacement was calculated as the product of average strain

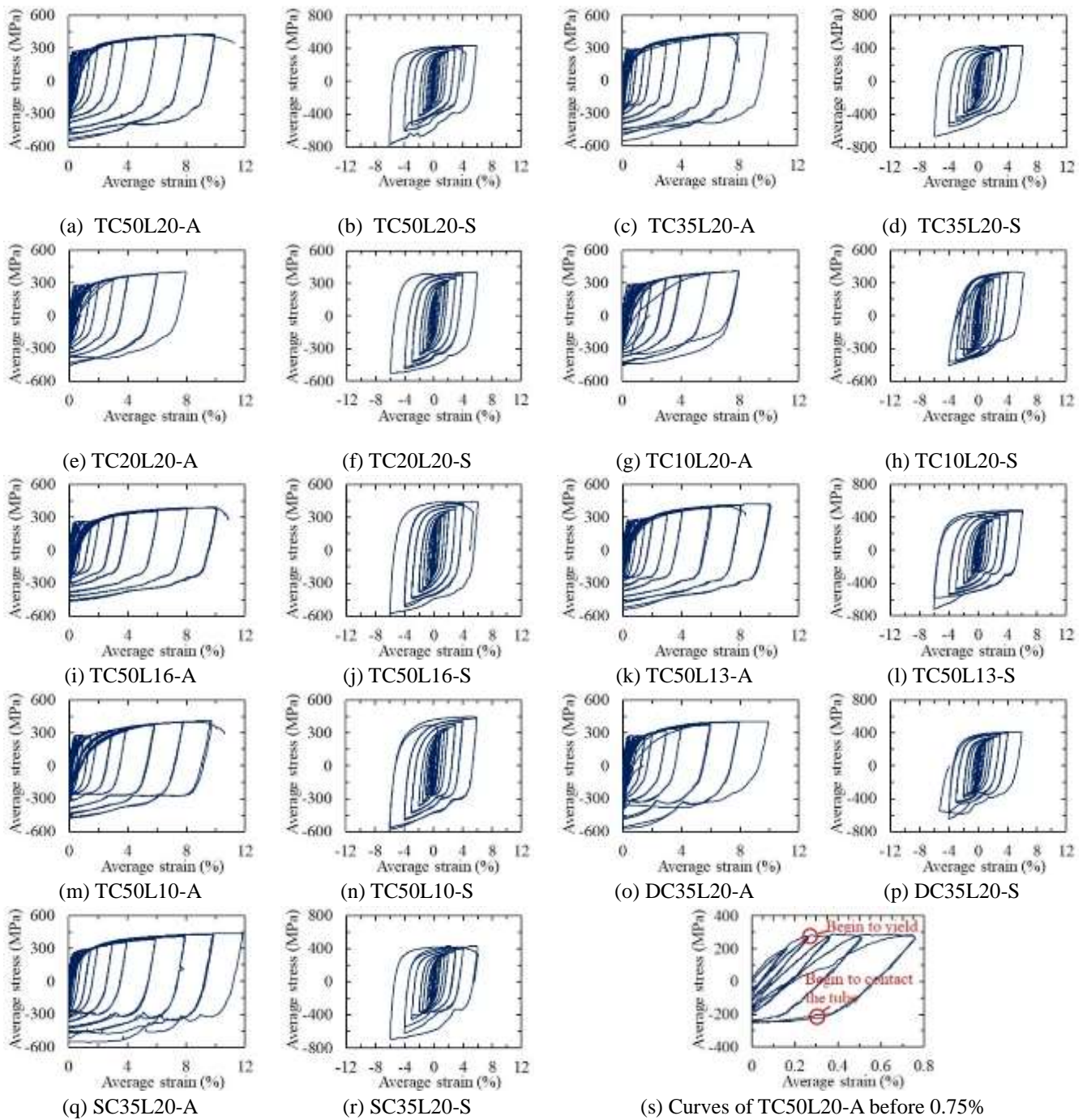


Fig. 8 Hysteretic curves

and length of the yielding portion. As shown in Fig. 7, the applied average strain increased gradually in an incremental form, and each amplitude was loaded twice. The increment of the amplitude remained 2% for the strain amplitude beyond 4%.

4. Numerical simulation

4.1 Hysteretic curves

Fig. 8 illustrates the hysteretic curves of the specimens, where the average strain is obtained as the ratio of the net displacement to the length of the yielding portion (L_d), and the stress is evaluated as the axial force divided by the minimum cross sectional area of the yielding portion.

Based on the hysteretic curves, it can be observed that all the specimens sustained the stages of elasticity, yielding and failure during the loading process. The hysteretic loop of the second cycle at each strain amplitude level was almost the same as the one of the first cycle without any apparent degradation. The average stress-average strain relationship of the specimens remained stable and smooth at the tensile half cycles, but became not smooth at the compressive ones. For the specimens under the asymmetric cyclic loading, the maximum tensile stress of each cycle was close to the maximum compressive stress. However, for the specimens under the symmetric cyclic loading, the maximum nominal compressive stress became much higher than the maximum tensile stress, especially for the several cycles before failure. This was due to the nonnegligible contact forces between the internal cores and the confining tubes, which will be further explained using numerical results in the subsequent section. Most of the specimens reached a maximum average tensile strain of 10% under the asymmetric loading history. Only Specimen TC20L20-A and TC10L20-A sustained a maximum average tensile strain of 8%. It is interesting to note that Specimen SC35L20-A, possessing inherent initial eccentricity, achieved the highest maximum average tensile strain of 12%. The specimens under the symmetric cyclic loading history failed at the maximum average strain of 6%, indicating much better deformation capacity than BRBs commonly with a deformation capacity less than 3%. In addition to the well-designed details, the high maximum ductility was also owing to the short length of the MBSFs compared with BRBs.

For better illustration of the hysteretic curves at initial loading amplitudes, the curves of Specimen TC50L20-A before an average strain of 0.75% are shown in Fig. 8(s). Most of the specimens began to yield at the tensile half cycle with a strain amplitude of 0.35%. For the specimens under the asymmetric loading protocol, the slopes of the compressive curves began to decrease gradually at the strain amplitude of 0.5% or 0.75% strain. The compressive stiffness of the specimens began to rise slightly during the cyclic loading process of 0.75% or 1.5% strain level. It can be inferred that the cores began to contact with the confining tubes at these strain amplitudes. Most of the specimens under the symmetric cyclic loading history buckled when the strain amplitude reached $\pm 0.35\%$, which can be inferred from the reduced slopes of the hysteretic curves at the compressive side. Likewise, it can be speculated that the confining tubes contacted with the cores at the $\pm 0.5\%$ strain amplitude. Compared with the other specimens, the core of Specimen SC35L20-S began to buckle and contact with the confining tube at a smaller strain amplitude level, indicating that the initial eccentricity contributed to its early buckling.

For the same gap size between the cores and the tubes, the loading head had to apply relatively larger loading displacements to the short specimens than the ones to the long specimens before contact between the cores and the confining tubes, which was resulted from the geometrical relationship. Therefore, the curves of specimens with shorter yielding portions exhibited curves of more apparent decreasing stiffness in the compressive half cycles.

Moreover, as shown in Fig. 8(m), the compressive stress of Specimen TC50L10-A decreased slightly during the course of increasing to the peak compressive stress of each cycle. The specimens of the single-cut cross section exhibited the most non-smooth compressive stress-strain relationship, followed by the double-cut cross sectional specimens, and the specimens of the quasi-triangular cross sections showed the most stable hysteretic properties under compression. This phenomenon indicated that the more symmetrical axes of the cross sections there were, the more smooth and stable performance of the MBSF specimens exhibited.

4.2 Failure modes

Fig. 9 depicts the failure modes of the specimens. There were 2 categories of failure modes, of which one was necking and subsequent rupture of the internal core. The other one was bending of the elastic portion near the movable end under compression, leading to significant contact force between the elastic portions and the external confining tubes. As to the first failure mode, tests were terminated due to sudden decrease of the tensile load-carrying capacity. As shown in Fig. 9, necking or rupture appeared between the mid-length of the yielding portions and the movable end. As the loads passed through the specimens, the friction, distributed on the contact points of the internal cores and the confining tubes longitudinally, transferred some loads to the confining tubes supported by the fixed end. Therefore, the portions between the necking or rupture locations and the fixed end bore relatively lower loads than the ones between the necking or rupture locations and the movable end. Due to the relatively higher compressive force, the portions of the cores between the necking or rupture location and the movable end showed more apparent residual buckling deformations than the rest portions, as shown in Fig. 9.

Specimens TC20L20-A, TC10L20-A, TC10L20-S, DC35L20-A, DC35L20-S and SC35L20-A failed due to bending of the elastic portions at the movable ends. There were no apparent residual buckling deformation in the yielding portions of Specimens TC20L20-A, TC10L20-A and TC10L20-S. This can be explained by the fact that the yielding portions of these specimens had relatively larger cross sectional area and thus higher compressive load-carrying capacity compared with the compressive yielding capacity of the unrestrained elastic portions. However, as shown in Figs. 9(o)-(q), Specimens DC35L20-A, DC35L20-S and SC35L20-A buckled in the yielding portions before bending of the elastic portions occurred, because the manufactured cross sections of these specimens were relatively smaller in areas.

4.3 Compression strength adjustment factor

There was no infilling material between the energy dissipation cores and the confining tubes of the newly proposed MBSFs, where only lubricant oil was employed and pasted on the surface of the internal cores. Based on the experimental results, the internal cores contacted with the confining tubes directly when the internal cores buckled,

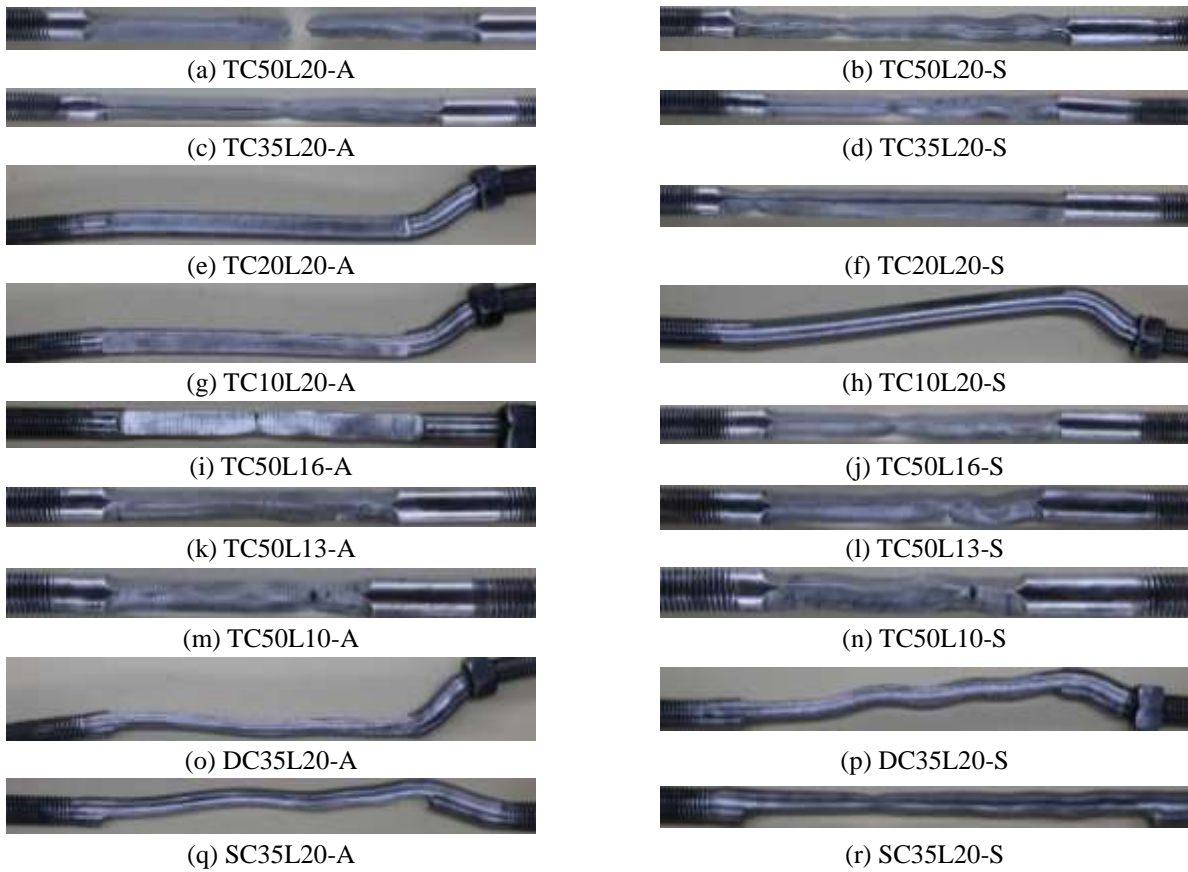
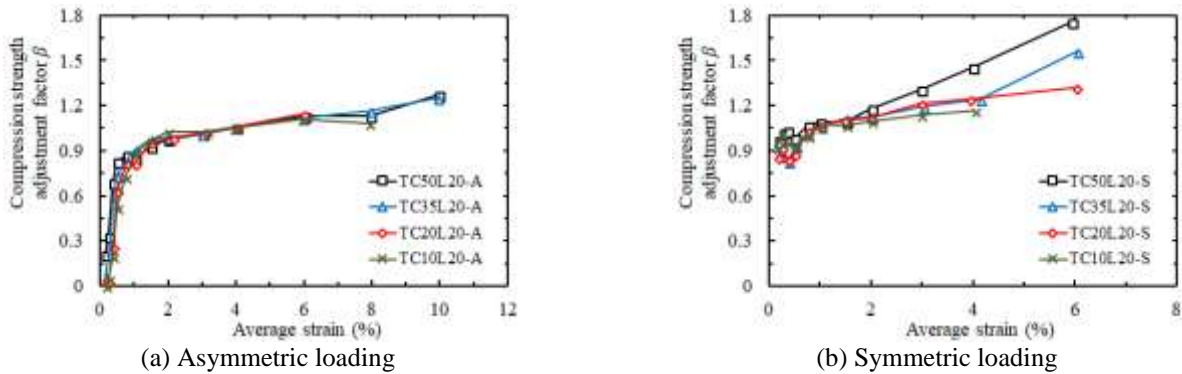
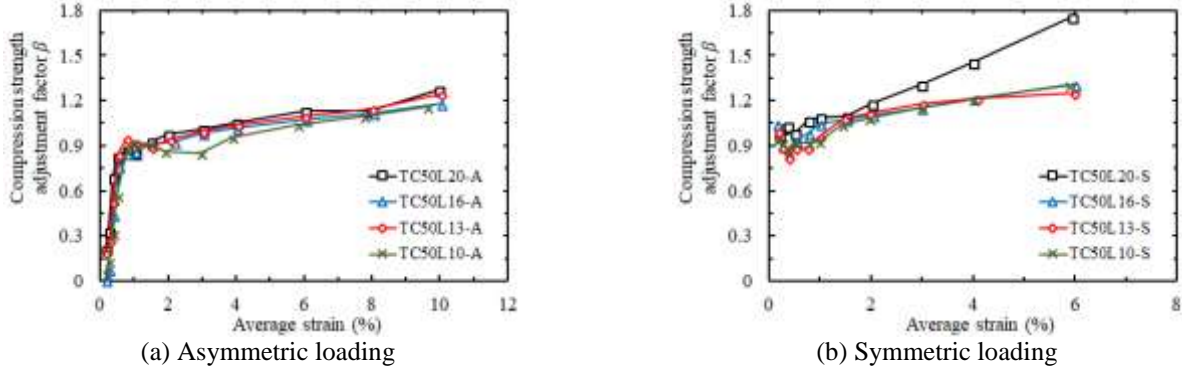
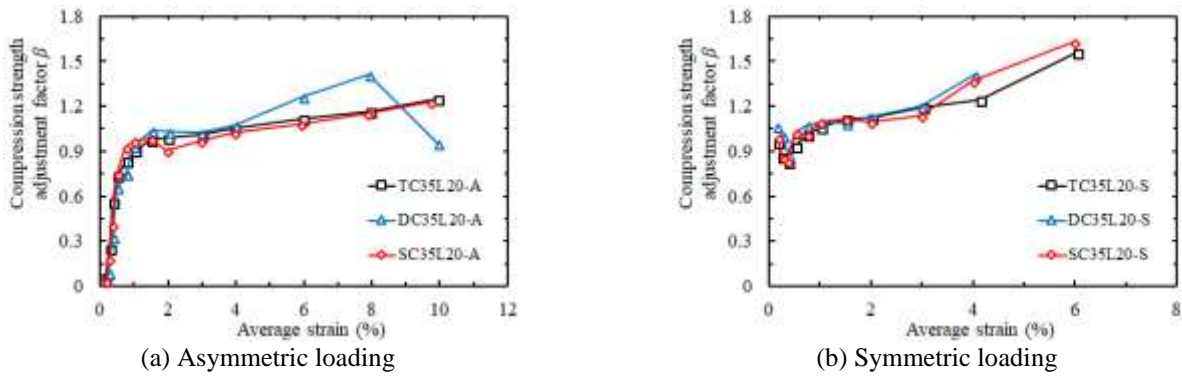


Fig. 9 Failure modes of tested specimens

Fig. 10 β of specimens with different R_a

leading to nonnegligible friction between the cores and the confining tubes. The compression strength adjustment factor, β , is considered as an appropriate index to evaluate the influence of the difference between the maximum compressive and the tensile axial force. In this study, β is calculated as the ratio of the peak average compressive stress to the peak average tensile stress at the first cycle of each strain amplitude. Figs. 10-12 illustrate the values of β for specimens with various R_a , length of the yielding portions and cross sectional types.

As the strain amplitude increased, β increased gradually. Most β of the specimens under the asymmetric cyclic loading was smaller than that of the corresponding specimens under the symmetric one, indicating the considerable friction in the specimens under the symmetric cyclic loading. The specimens under the asymmetric cyclic loading, except Specimen DC35L20-A, exhibited β below 1.3, satisfying the criterion in AISC 341-10 (AISC341-10 2010). As shown in Figs. 10(b) and 11(b), the maximum β of the specimens except TC50L20-S remained lower than the threshold value of 1.3 before the strain amplitude level

Fig. 11 β of specimens with different lengthFig. 12 β of specimens with different cross sectional types

of 4%. Thus, it can be inferred that the proposed MBSFs can be applied to symmetric cyclic loading occasions, where the maximum strain was designed below 4%.

4.4 Ductility and dissipated energy

Ductility indicates the inelastic deformation capacity of fuses to absorb energy induced by seismic excitations without remarkable strength loss. There are 2 kinds of indices used to evaluate the ductility capacity of fuses, one refers to the maximum ductility, μ_{\max} , defined as the ratio of the peak deformation to the yield deformation, and the other is related to the cumulative energy dissipation capacity. The latter can either be expressed by the cumulative ductility index, μ_c , or the cumulative inelastic deformation (CID). The μ_c and CID are respectively given by Eqs. (2) and (3).

$$\mu_c = \sum \frac{\varepsilon_{u,i}}{\varepsilon_y} \quad (2)$$

$$CID = \sum (\varepsilon_{u,i} - \varepsilon_y)$$

where $\varepsilon_{u,i}$ is the peak average strain of specimens at the i -th loading cycle, ε_y is the nominal yielding strain of specimens. Table 4 gives the values of μ_{\max} , μ_c , CID and the total energy dissipated by the specimens.

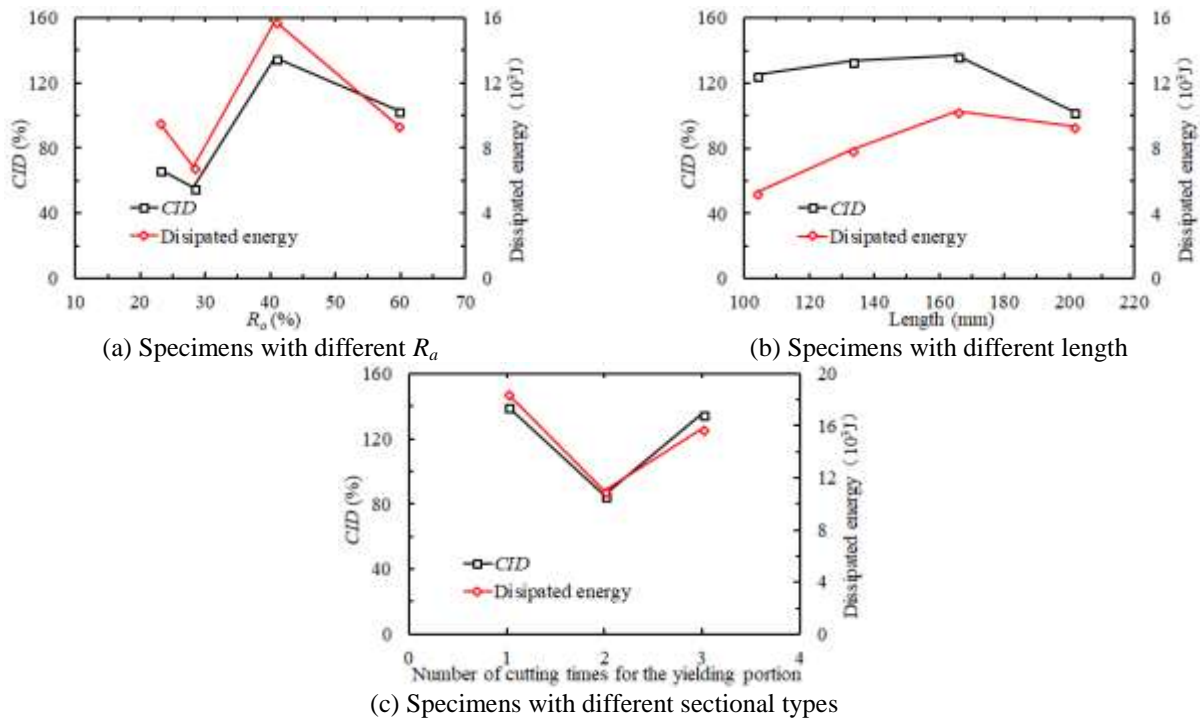
The specimens under the asymmetric cyclic loading showed much higher μ_{\max} than the corresponding ones under the symmetric cyclic loading. Except Specimens TC10L20-A and TC10L20-S, μ_c of the specimens under the asymmetric cyclic loading was comparable with or marginally higher than those of the corresponding ones under the symmetric loading. The specimens, except Specimens TC20L20-A, TC10L20-A and TC10L20-S, showed much higher cumulative ductility indices than the threshold value of 200, satisfying the demand in AISC 341-10 (AISC341-10 2010). Because of the relatively higher yield strength of Specimens TC20L20-A, TC10L20-A and TC10L20-S, the total yield deformations of the three specimens were relatively large. In addition, premature bending of the elastic portions also led to relatively low displacement capacities of Specimens TC20L20-A, TC10L20-A and TC10L20-S. Therefore, the values of μ_c for these three specimens were lower than the threshold value of 200. Most CIDs of specimens exceeded 100%, which were even higher than the requirement for high-performance BRBs (Jia *et al.* 2017, Jia *et al.* 2018a, b, Jia *et al.* 2019).

The results of CIDs and total dissipated energy for specimens with different design parameters are plotted in Figs. 13 and 14. It can be observed that CID was related to the energy dissipation capacity, and a higher CID corresponded to a better energy dissipation capacity. In general, the specimens with a R_a of around 40% exhibited

Table 4 Ductility capacity and energy dissipation capacity of specimens

No.	Specimens	μ_{\max}	μ_c	CID (%)	Dissipated energy (kJ)	Maximum ζ_{eq}
1	TC50L20-A	37.2	273.9	103.1	9389.1	0.48
2	TC50L20-S	22.6	266.8	114.5	10822.7	0.44
3	TC35L20-A	40.0	306.8	135.4	15821.6	0.46
4	TC35L20-S	21.3	243.8	113.3	12537.1	0.46
5	TC20L20-A	20.2	122.5	55.8	6823.2	0.43
6	TC20L20-S	19.8	219.6	108.7	14409.0	0.49
7	TC10L20-A	20.9	145.9	67.2	9584.5	0.45
8	TC10L20-S	15.2	185.5	85.0	11925.7	0.44
9	TC50L16-A	35.6	306.6	137.2	10263.1	0.47
10	TC50L16-S	23.3	276.3	116.7	9439.9	0.48
11	TC50L13-A	32.7	276.7	133.7	7925.3	0.46
12	TC50L13-S	20.5	266.3	131.7	7778.4	0.48
13	TC50L10-A	32.4	261.3	128.5	5296.2	0.44
14	TC50L10-S	20.6	267.9	130.3	5553.4	0.46
15	DC35L20-A	31.9	306.8	85.5	11037.5	0.47
16	DC35L20-S	20.8	210.4	87.3	11278.7	0.44
17	SC35L20-A	39.1	302.5	139.9	18464.6	0.48
18	SC35L20-S	21.0	251.5	114.8	15137.6	0.46

Notes: μ_{\max} = ratio of peak deformation to yielding deformation, μ_c = cumulative ductility, CID = sum of average plastic strain of the yielding portions, ζ_{eq} = equivalent viscous damping ratio

Fig. 13 CID and total dissipated energy of specimens under asymmetric loadings

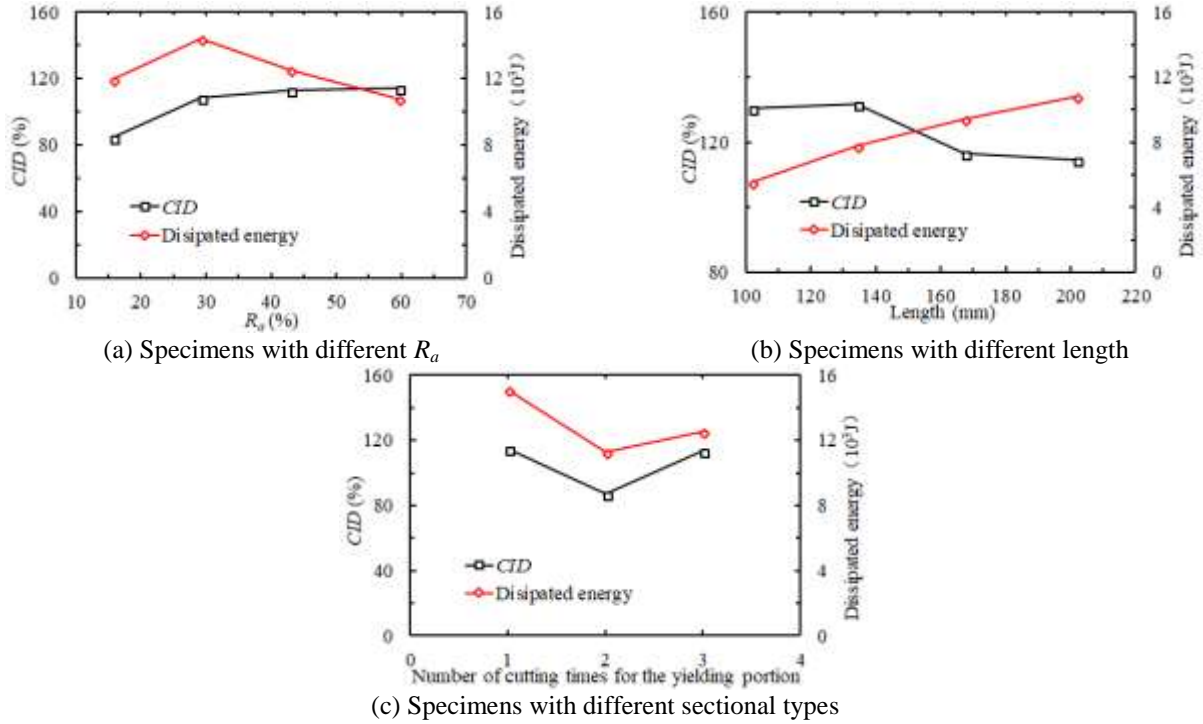


Fig. 14 CID and total dissipated energy of specimens under symmetric loadings

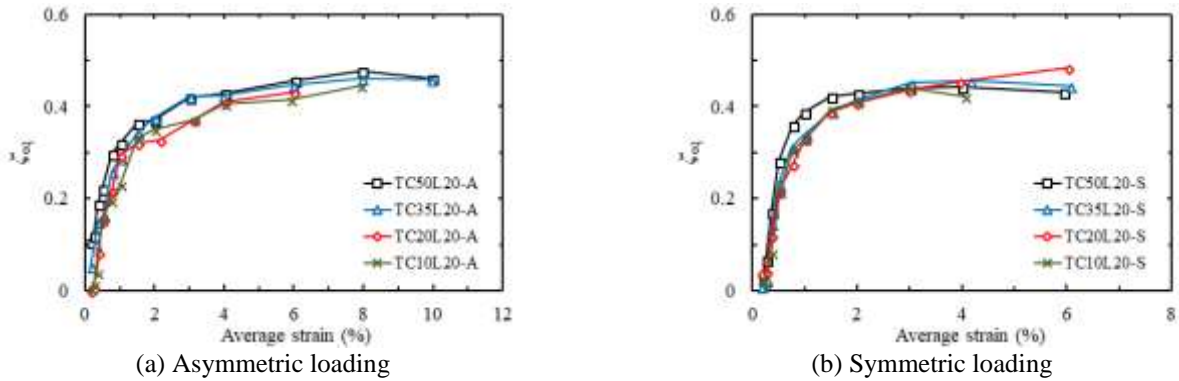
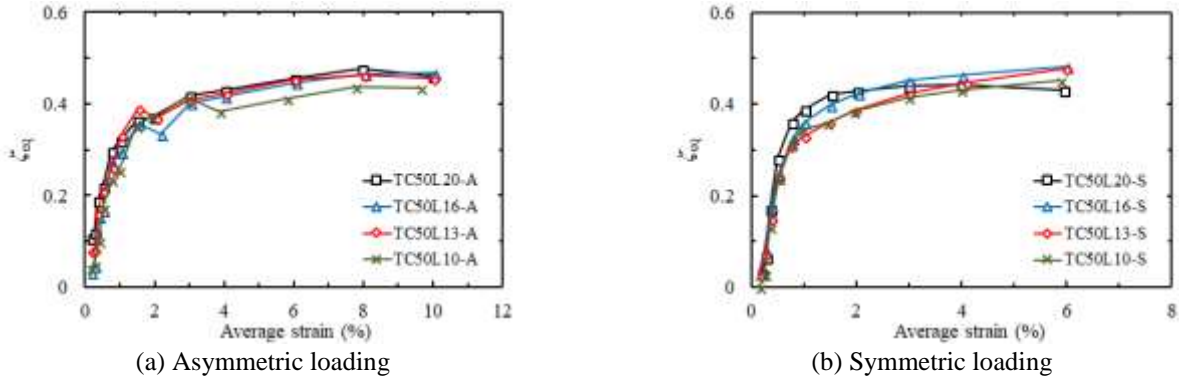
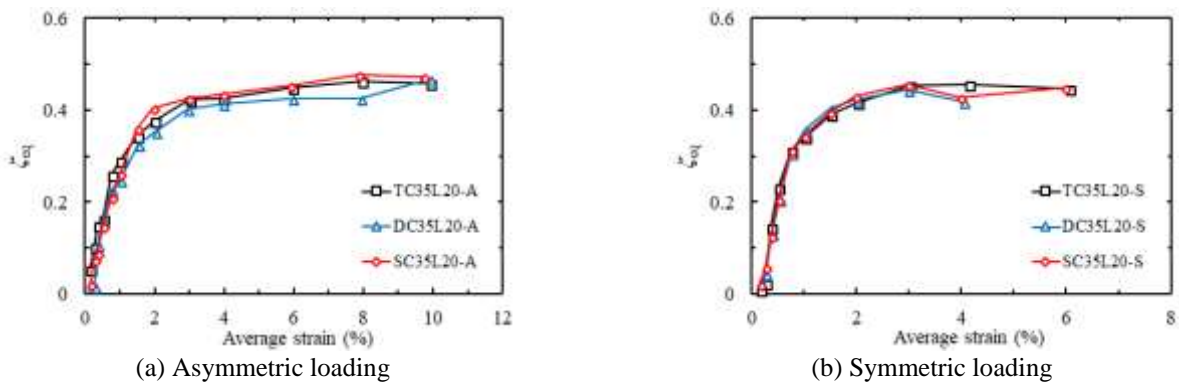


Fig. 15 ζ_{eq} of specimens with different R_a

good ductility and energy dissipation capacities. Comparing the specimens of different lengths, it was found that the total dissipated energy increased with an increasing length of the yielding portion. The specimens with a length of 130 mm showed relatively high ductility under both the asymmetric and the symmetric cyclic loadings. Among the specimens of different cross sectional types, the single-cut cross sectional specimens achieved the highest CID and dissipated energy under both the asymmetric and symmetric cyclic loadings. It can be attributed to the relatively larger gaps between the single-cut side and the confining tube, allowing the single-cut cores to generate the total longitudinal deformation with relatively lower strain.

4.4 Equivalent viscous damping ratio

Equivalent viscous damping ratio, ζ_{eq} , is an important variable to analyze seismic responses of structures or components, which also reveals the pinching effect of the hysteretic loops. Relatively higher equivalent viscous damping ratio represents better energy dissipation capacity in a single loop. The ζ_{eq} is defined as the ratio of dissipated energy in one cycle to the strain energy of an equivalent linear system that is multiplied by 2π . The maximum ζ_{eq} is listed in Table 4, and Figs. 15-17 show the relationships of ζ_{eq} versus the strain amplitude. The plotted ζ_{eq} was calculated based on the first hysteretic loop at each strain amplitude to study the effect of different parameters.

Fig. 16 ζ_{eq} of specimens with different lengthFig. 17 ζ_{eq} of specimens with different cross sectional types

The maximum ζ_{eq} of the specimens ranged from 0.43 to 0.49, comparable with those of BRBs (Wang *et al.* 2017). With an increasing strain amplitude, ζ_{eq} increased before the strain amplitude of 2% was achieved, after which ζ_{eq} tended to remain at a stable value. The specimens with a larger R_a corresponded to a larger ζ_{eq} . For the specimens with different lengths, ζ_{eq} decreased with a reducing length of the yielding portion. The values of ζ_{eq} for the single-cut cross sectional specimens ranked the first in the 3 cross sectional types.

5. Numerical simulation

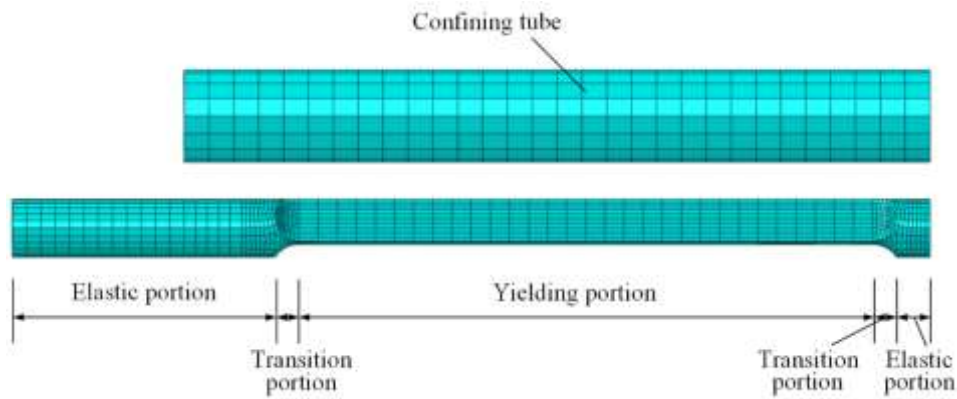
5.1 Numerical modeling

To investigate the buckling modes and failure mechanism of the newly proposed MBSFs, finite element (FE) models were established for 2 representative specimens, i.e., TC50L20-A and TC50L20-S, using ABAQUS (ABAQUS 2013). Reduced integration elements (C3D8R) were employed to simulate the behavior of the 2 specimens, considering cyclic plasticity, contact and ductile fracture. As illustrated in Fig. 18(a), different portions were meshed with different element sizes. The left end was coupled with a reference point constrained in the directions perpendicular to the core, on which a displacement loading history was applied. The right end was tied to a fixed elastic

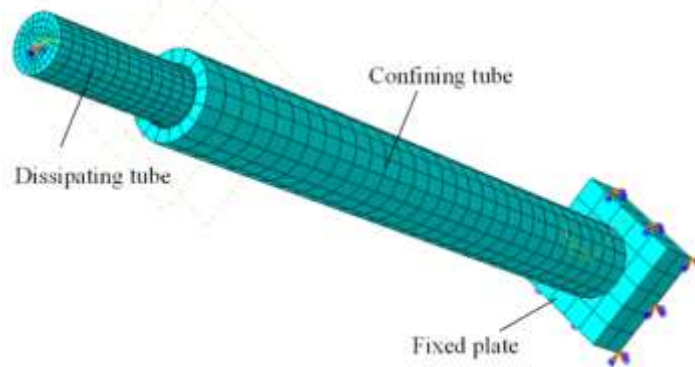
steel plate to simulate the boundary condition in the experiments. The confining tube was connected to the fixed end plate with the “hard contact” to simulate the real boundary condition of the confining tube, as shown in Fig. 18(b). The interaction of the core and the tube was also defined as “hard contact” with a frictional coefficient of 0.2 (Chen *et al.* 2016). A nonlinear combined hardening rule was employed for the steel based on the coupon tests. Based on the model developed by (Xiang *et al.* 2017), the maximum enlargement of the yield surface and the material parameter related to the isotropic hardening rate were defined as 154.87 MPa and 7.6, respectively. The ductile fracture model developed by Jia *et al.* (Jia *et al.* 2014, Jia and Kuwamura 2014a, b, Jia and Kuwamura 2015, Ping *et al.* 2017) was utilized to simulate ductile cracking of the cores under cyclic loading. The critical void growth index, χ_{cr} , was assumed as 2.25 (Kato *et al.* 2015). The initial geometric imperfection based on the first buckling mode of the core was employed with a maximum magnitude equal to 1/1000 of the core length.

5.2 Numerical results

The average stress versus average strain curves of the FE analysis results are compared with the experimental ones in Fig. 19. It can be seen that the hysteretic behaviors of TC50L20-A and TC50L20-S were well evaluated by the numerical simulation. Fracture occurred at the central range

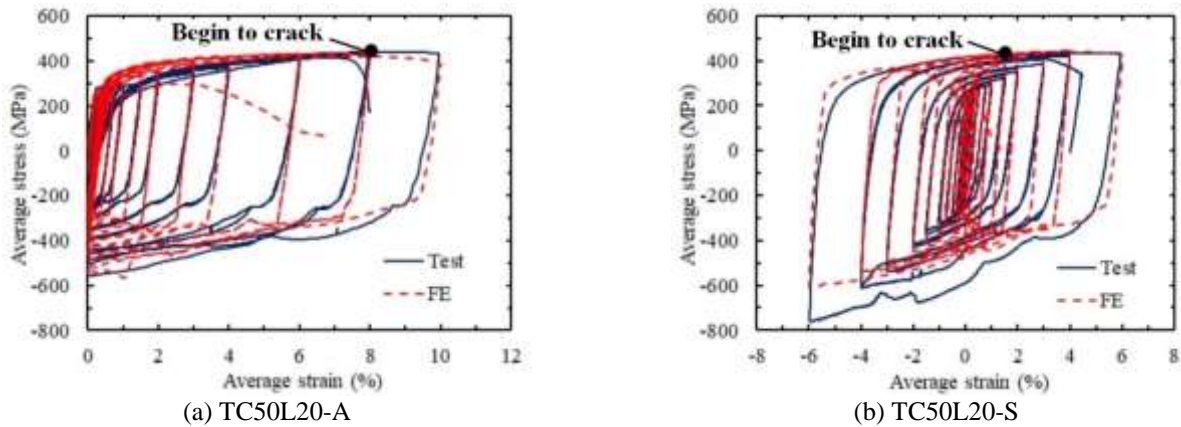


(a) Element sizes of different portions



(b) Assembly of components

Fig. 18 FE model of specimen



(a) TC50L20-A

(b) TC50L20-S

Fig. 19 Comparison of experimental and numerical results

of the yielding portions as shown in Fig. 20. The cores under the asymmetric loading and the symmetric loading began to crack at the second loading cycle of the 8% strain amplitudes and the first loading cycle of 6% strain amplitudes, which can be considered as the deformation limit of the proposed MBSFs, respectively.

The remaining arc parts of the yielding portion played an important role in restraining the buckling deformation of the yielding portion at the movable end, which was proved based on the considerable contact stress between the yielding portion and the internal side of the confining tube. The FE analysis results also indicated that the contact force between the elastic portion and the inner edge of the confining tube end was much greater than the one between the yielding portion and the tube, especially when the

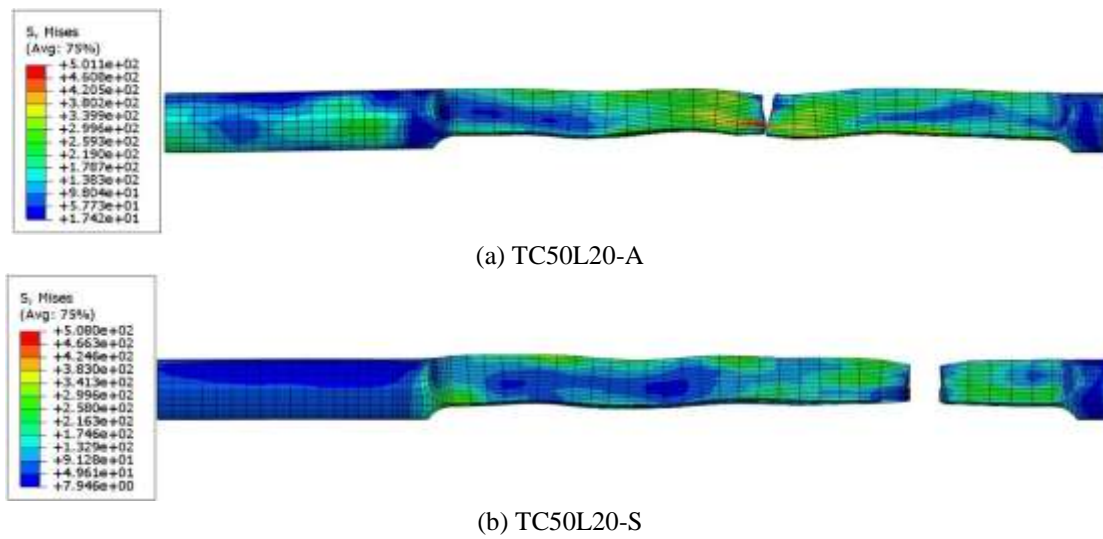


Fig. 20 Mises stress and failure mode of TC50L20-A and TC50L20-S



Fig. 21 Contact stress of TC50L20-A at average strain amplitude of 10%

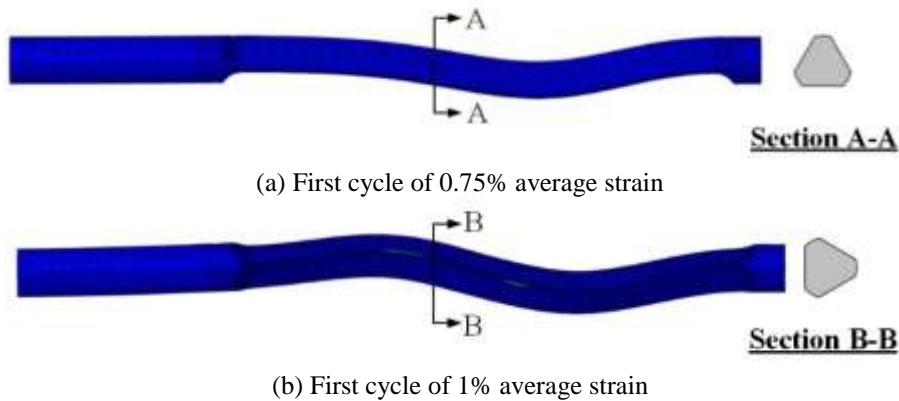


Fig. 22 Deformation modes of core for Specimen TC50L20-A

specimen was subjected to large compressive strain loading. Fig. 21 shows the contact stress distribution of the core in TC50L20-A at the compressive average strain amplitude of 10%. It can be concluded that the contact between the elastic portion and the inner edge of the confining tube end was a nonnegligible factor affecting the behavior of the newly proposed MBSF. The details in the inner edge of the confining tube end should be filleted to mitigate the contact stress.

Fig. 22 gives the deformation of the core in Specimen TC50L20-A when the core firstly contacted the confining tube, which was amplified by 10 times for better illustration. At the strain amplitude of 0.75%, the core of TC50L20-A began to buckle in the first mode along the axis of symmetry direction, as shown in Fig. 22(a). At the first cycle of the 1% strain amplitude, the core contacted with the tube in the direction perpendicular to the axis of symmetry near the moveable end, as illustrated in Fig. 22(b). It can be concluded that the core deformed in a spatial mode and hysteretic performance was influenced by deformation modes in the different directions.

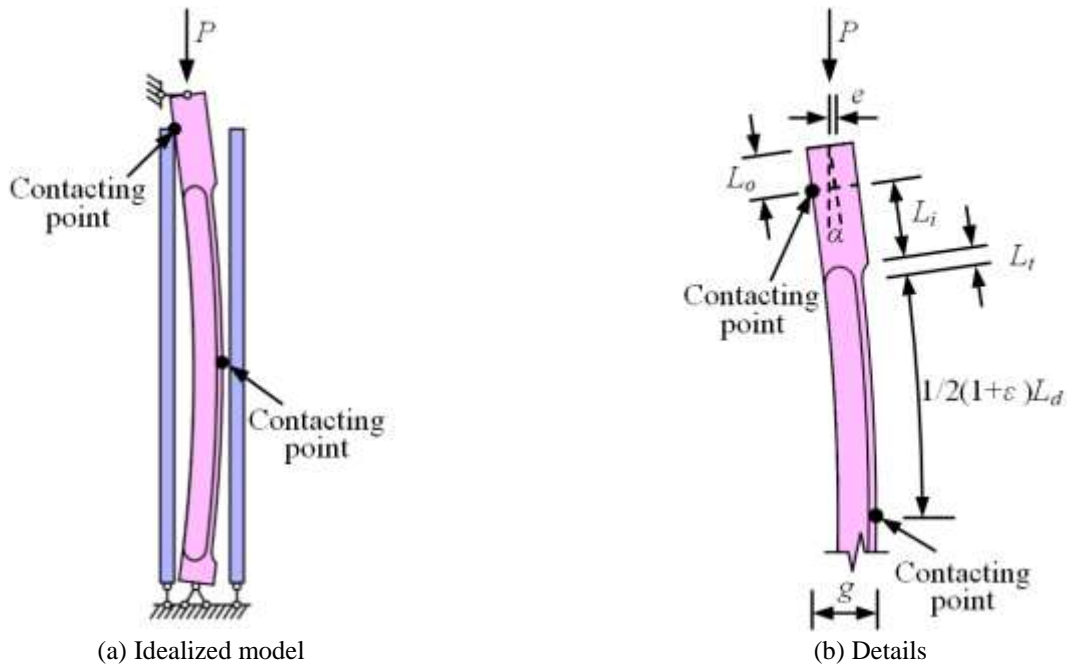


Fig. 23 Analytical model to evaluate bending of elastic portions

6. Design recommendations based on experimental and numerical results

6.1 Structural details of MBSFs

Compared with the designed configurations, there were undesirable manufacturing deviations in the central cores of the tested specimens, as shown in Table 2. However, most of the specimens can achieve stable and satisfying hysteretic performances based on the experimental results. This demonstrates that the structural details of the newly proposed MBSFs are effective with high robustness. The thread portions of all the specimens, including the ones with the smallest value of R_a , i.e., 15.7%, exhibited no damage or plastic deformation during the whole loading test. Thus, it is an ideal method to produce the connecting zones for the newly proposed MBSFs by the thread rolling process, which is economic, convenient, time-efficient and with high elastic strength to avoid net section failure. The contact between the elastic portion and the inner edge of the confining tube end considerably affects the compressive behavior of the proposed MBSFs. Structural measures, e.g., grinding the inner edge of the tube end, may be necessary to eliminate or reduce this influence. In addition, using high-performance unbonding material may be an alternative approach to solve this problem.

Comparing the number of sectional axis of symmetry, the quasi-triangular section is the most symmetrical among the 3 cross sectional types. Because the specimens of the quasi-triangular cross section produced more stable hysteresis loops than the double-cut and single-cut specimens, a conclusion can be drawn that the higher symmetric degree of the cross section is, the more smoothly and stably the newly proposed MBSFs behave. Therefore, the quasi-triangular section is confirmed as a proper cross

sectional type. Considering the indices of the CID , total dissipated energy and equivalent viscous damping ratio, the specimens with a R_a of around 40% exhibited high efficiency, making this value the optimum design of the MBSFs. Since longer yielding portions leads to larger energy dissipation, the length of the yielding portions, suitable for applied occasions, should be relatively large to obtain more satisfying hysteretic performance, where it should be also noted that the initial stiffness of the beam-column connections is also significantly dependent on the length of the yielding portions and the global buckling should be also considered in real applications.

6.2 Ultimate design strain

Under the asymmetric cyclic loading, all the specimens can produce a maximum tensile average strain beyond 8%. Moreover, the strain amplitude of 10% was sustained by most of the specimens. In addition, the FE simulation revealed that the specimen began to crack slightly at the second cycle of 8%. Based on this fact, it is suitable to employ 8% as the ultimate design strain of the newly proposed MBSFs under the asymmetric cyclic loading. As to the specimens under the symmetric cyclic loading, the compression strength adjustment factors maintained under the criterion of 1.3 before the cyclic loading strain reached 4%. Thus, 4% is recommended as the ultimate design strain of the newly proposed MBSFs under the symmetric cyclic loading. With an appropriate beam height, the suggested ultimate design strain of MBSFs can be adopted in the steel and precast hybrid concrete connections intended for CP performance.

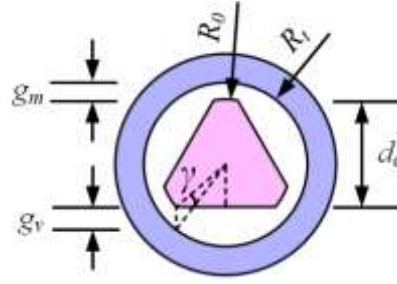


Fig. 24 Critical parameters defining lateral deformation of yielding portion

6.3 Discussion of elastic portions

It can be concluded from the test results that the elastic portions play an important role in failure modes of the tested specimens. The bending of the elastic portions will reduce the overall performance of the MBSFs significantly. Therefore, the elastic portions should not yield during buckling of the cores. In other words, the load-bearing capacity of the elastic portion should be higher than the ultimate compressive capacity of the yielding portion. To calculate the load-bearing capacity of the elastic portion, the core is assumed to bend in a circular-arc shape restrained by the contact points at the inner edge of the tube end and the mid-length of the core, as shown in Fig. 23(a). Considering the weak constraining of the nuts, the ends of the two elastic portions are idealized as hinges. To simplify the analytical process, the strain of the elastic and transition portions are not included in the calculation method in this section. Moreover, to obtain a safer design value, the length of the yielding portions used in the calculation, is considered as the elongated length at the ultimate tensile design strain. As illustrated in Fig. 23(b), the long elastic portion sustains both the compression and the moment produced by the applied load and the eccentricity, which is caused by the deformed configuration.

When the core contacts the inner edge of the tube end, bending of the elastic portion outside the confining tube initiates. The maximum stress of the core at the location corresponding to the inner edge of the tube end is obtained by Eq. (4)

$$\sigma_m = \frac{4P}{\pi d_o^2} + \frac{32Pe}{\pi d_o^3} \quad (4)$$

where σ_m is the maximum stress of the elastic portion corresponding to the inner edge of the tube end, d_o is the diameter of elastic portions, P is the applied force, and e is the eccentricity of the applied force relative to the center of the elastic portion section. The eccentricity is calculated by Eq. (5)

$$e = L_o \sin \alpha \approx L_o \alpha \quad (5)$$

where L_o is the length of the elastic portion outside the confining tube, α is the rotating angle due to buckling of the yielding portion. As the buckling shape of the yielding portion is assumed as a circular arc, α can be computed

based on the geometrical relationship as Eq. (6)

$$1/2(1+\varepsilon)L_d(1-\cos \alpha)/\alpha + (L_i + L_i) \sin \alpha = g \quad (6)$$

where ε is the average tensile strain, L_i is the length of the elastic portion inside the confining tube, g is the lateral distance of the 2 contact points which is determined by the gaps between the core and the confining tube, as shown in Fig. 24.

It can be seen that g is comprised of the minimum distances of the remaining arc and the cut edges to the confining tube, which are calculated based on Eqs. (7)-(9)

$$g_m = R_i - R_o \quad (7)$$

$$R_i^2 = R_o^2 + g_v^2 - 2R_o g_v \cos(\gamma + \frac{\pi}{2}) \quad (8)$$

$$\sin \gamma = (d_e - R_o) / R_o \quad (9)$$

where g_m is the minimum distance between the remaining arc and the confining tube, R_i and R_o are the inner radius of the tube and radius of the raw steel bar, respectively, g_v is the distance between the cut edges and the tube in the axis of symmetry direction, γ is the angle related to the cut edge in the triangular of the yielding portion as shown in Fig. 24.

Based on Eqs. (4)-(9), the theoretical compressive loads corresponding to yielding of the elastic portions were calculated for the tested specimens with quasi-triangular section, as listed in Table 5. σ_m was considered as the yield strength obtained from coupon tests. ε was assigned as 8% and 4% for the asymmetric and symmetric loadings, respectively. Considering the preliminary design method of the MBSF that is analogical to the one of BRBs, the experimental compressive loads are also listed in Table 5, which were obtained by multiplying the ultimate tensile loads with the compression strength adjustment factor, β , where an allowed maximum value of 1.3 is adopted, as stipulated in AISC 341-10 (AISC341-10 2010).

It can be seen that the calculated compressive loads, which corresponded to yielding of the elastic portions, were smaller than the experimental results, because the boundary conditions were idealized as hinges in the analytical models. The real boundary conditions provided by the nuts were difficult to evaluate precisely. However, it was found that

Table 5 Calculated applied loads and experimental results

No.	Specimen	P_{exp} (kN)	P_{cal} (kN)	P_{cal}/P_{exp}	Failure modes
1	TC50L20-A	64.96	56.56	0.87	Necking of yielding portions
2	TC50L20-S	72.81	62.25	0.86	Necking of yielding portions
3	TC35L20-A	96.24	58.04	0.60	Necking of yielding portions
4	TC35L20-S	91.91	63.54	0.69	Necking of yielding portions
5	TC20L20-A	108.93	59.27	0.54	Bending of elastic portions
6	TC20L20-S	111.46	64.60	0.58	Necking of yielding portions
7	TC10L20-A	123.60	60.31	0.49	Bending of elastic portions
8	TC10L20-S	131.56	65.49	0.50	Bending of elastic portions
9	TC50L16-A	78.09	56.41	0.72	Necking of yielding portions
10	TC50L16-S	83.40	61.54	0.74	Necking of yielding portions
11	TC50L13-A	74.46	56.25	0.76	Necking of yielding portions
12	TC50L13-S	77.77	60.72	0.78	Necking of yielding portions
13	TC50L10-A	72.38	56.04	0.77	Necking of yielding portions
14	TC50L10-S	74.80	59.73	0.80	Necking of yielding portions

Notes: P_{exp} = experimental compressive loads, P_{cal} = calculated compressive loads

the specimens with P_{cal}/P_{exp} higher than 0.58 failed in the desirable mode, i.e., necking and rupture of the yielding portions. Therefore, the proposed analytical model can be employed to evaluate and design the elastic portions by adding an adjustment factor. An adjustment factor, η , was proposed to estimate the influence of boundary conditions based on the experimental results. The elastic portions should be designed to satisfy Eq. (10)

$$P_{cal} \geq \eta \beta P_t \quad (10)$$

where P_t = design ultimate tensile strength of the MBSFs, η = boundary condition adjustment factor, where a value of 0.6 is suggested based on the above discussions.

6. Design recommendations based on experimental and numerical results

A miniature bar-type structural fuse (MBSF) with cold formed bolted connections was introduced in this paper, aiming to promote massive applications with simple and cost-effective manufacturing details while satisfying seismic performance. The effects of the cross sectional type, loading history, length of the yielding portion and cut cross sectional area ratio were investigated. Three different cross sections were studied, i.e., triple-cut, double-cut and single-cut cross sections. Totally 18 specimens were tested under both asymmetric and symmetric cyclic loading histories to investigate hysteretic behaviors of the newly proposed MBSFs. Numerical simulation of 2 representative specimens were also conducted. Based on the results, conclusions can be drawn as follows:

1. Most of the MBSF specimens achieved stable and satisfying hysteretic performance based on the experimental results, demonstrating effectiveness of the structural details in the MBSFs.

2. The triple-cut specimens with quasi-triangular cross sections were considered as the most symmetrical type based on the number of sectional axis of symmetry. The hysteretic curves of these specimens at compressive loading half cycles were found to be the most stable. Thus, the quasi-triangular cross section is confirmed to be the recommended cross sectional type.

3. The MBSF specimens exhibited a satisfactory ductility capacity. An average strain of 8% and 4% is respectively recommended as the ultimate design strain of the MBSFs for the asymmetric and symmetric loading histories.

4. Based on the ductility and energy dissipation capacity, the cut cross sectional area ratio, R_a , of around 40% is recommended for MBSFs.

5. Experimental and numerical simulation indicated that contact between the elastic portion of the core and the end of the confining tube can lead to premature failure at the elastic portion. An analytical model to evaluate the bending failure at the elastic portion is proposed, and a design method to avoid this failure mode is also presented.

Acknowledgements

This work was supported by the Key R&D Program of China (No. 2017YFC0703607, No. 2016YFC0701703), National Natural Science Foundation of China (No. 51678136, No. 51508401 and No. 51808109), the Fundamental Research Funds for the Central Universities, and the Natural Science Foundation of Jiangsu (BK20180385).

References

- ABAQUS (2013), ABAQUS/Analysis User's Manual-version 6.13. Inc., Pawtucket, Rhode Island.
- AISC341-10 (2010), Seismic provisions for structural steel buildings, American Institute of Steel Construction, Chicago, Illinois.
- Amaris Mesa, A. (2010), "Developments of advanced solutions for seismic resisting precast concrete frames", Ph.D. Thesis; University of Canterbury, Christchurch, New Zealand.
- ASCE41-06 (2007), Seismic rehabilitation of existing buildings, American society of civil engineers, Reston, VA.
- Calado, L., Proenca, J.M., Espinha, M. and Castiglioni, C.A. (2013), "Hysteretic behavior of dissipative welded fuses for earthquake resistant composite steel and concrete frames", *Steel Compos. Struct.*, **14**(14), 547-569. <https://dx.doi.org/10.12989/scs.2013.14.5.547>.
- Chen, Q., Wang, C.L., Meng, S. and Zeng, B. (2016), "Effect of the unbonding materials on the mechanic behavior of all-steel buckling-restrained braces", *Eng. Struct.*, **111**, 478-493. <https://doi.org/10.1016/j.engstruct.2015.12.030>.
- Christopoulos, C., Filiatrault, A., Uang, C.M. and Folz, B. (2002), "Posttensioned energy dissipating connections for moment-resisting steel frames", *J. Struct. Eng.*, **128**(9), 1111-1120. [https://doi.org/10.1061/\(ASCE\)0733-9445\(2002\)128:9\(1111\)](https://doi.org/10.1061/(ASCE)0733-9445(2002)128:9(1111)).
- Fleischman, R.B. and Seeber, P.E.K. (2016), "New construction for resilient cities: the argument for sustainable low damage precast/prestressed concrete building structures in the 21st century", *Sci. Iran.*, **23**(4), 1578-1593.
- Ghosh, S.K., Nakaki, S.D. and Krishnan, K. (1997), "Precast structures in regions of high seismicity: 1997 UBC design provisions", *PCI J.*, **42**(6), 76-91.
- Gorgun, H. (2018), "An experimental study of the behaviour of double sided bolted billet connections in precast concrete frames", *Steel Compos. Struct.*, **29**(5), 603-622. <https://doi.org/10.12989/scs.2018.29.5.603>.
- Guan, D., Guo, Z., Xiao, Q. and Zheng, Y. (2016), "Experimental study of a new beam-to-column connection for precast concrete frames under reversal cyclic loading", *Adv. Struct. Eng.*, **19**(3), 529-545. <https://doi.org/10.1177/1369433216630122>.
- Guan, D., Jiang, C., Guo, Z. and Ge, H.B. (2018), "Development and seismic behavior of precast concrete beam-to-column connections", *J. Earthq. Eng.*, **22**(2), 234-256. <https://doi.org/10.1080/13632469.2016.1217807>.
- Huang, S. (2016), "Research on mechanical connection of 500 MPa high strength rebars", M.S. Thesis; Nanjing University of Aeronautics and Astronautics, Nanjing, China. (In Chinese)
- Jia, L.J., Dong, Y., Ge, H.B., Kondo, K. and Xiang, P. (2019), "Experimental study on high-performance buckling-restrained braces with perforated core plates", *Int. J. Struct. Stab. D.*, **19**(1), 1940004. <https://doi.org/10.1142/S0219455419400042>.
- Jia, L.J., Ge, H.B., Maruyama, R. and Shinohara, K. (2017), "Development of a novel high-performance all-steel fish-bone shaped buckling-restrained brace", *Eng. Struct.*, **138**, 105-119. <https://doi.org/10.1016/j.engstruct.2017.02.006>.
- Jia, L.J., Ge, H.B., Xiang, P. and Liu, Y. (2018a), "Seismic performance of fish-bone shaped buckling-restrained braces with controlled damage process", *Eng. Struct.*, **169**, 141-153. <https://doi.org/10.1016/j.engstruct.2018.05.040>.
- Jia, L.J., Li, R.W., Xiang, P., Zhou, D.Y. and Dong, Y. (2018b), "Resilient steel frames installed with self-centering dual-steel buckling-restrained brace", *J. Constr. Steel Res.*, **149**, 95-104. <https://doi.org/10.1016/j.jcsr.2018.07.001>.
- Jia, L.J., Koyama, T. and Kuwamura, H. (2014a), "Experimental and numerical study of postbuckling ductile fracture of heat-treated SHS stub columns", *J. Struct. Eng.*, **140**(7), 04014044. [https://doi.org/10.1061/\(ASCE\)ST.1943-541X.0001056](https://doi.org/10.1061/(ASCE)ST.1943-541X.0001056).
- Jia, L.J. and Kuwamura, H. (2014b), "Ductile fracture simulation of structural steels under monotonic tension", *J. Struct. Eng.*, **140**(5), 04013115. [https://doi.org/10.1061/\(ASCE\)ST.1943-541X.0000944](https://doi.org/10.1061/(ASCE)ST.1943-541X.0000944).
- Jia, L.J. and Kuwamura, H. (2014), "Prediction of cyclic behaviors of mild steel at large plastic strain using coupon test results", *J. Struct. Eng.*, **140**(2), 04013056. [https://doi.org/10.1061/\(ASCE\)ST.1943-541X.0000848](https://doi.org/10.1061/(ASCE)ST.1943-541X.0000848).
- Jia, L.J. and Kuwamura, H. (2015), "Ductile fracture model for structural steel under cyclic large strain loading", *J. Constr. Steel Res.*, **106**, 110-121. <https://doi.org/10.1016/j.jcsr.2014.12.002>.
- Kato, T., Jia, L.J. and Ge, H.B. (2015), "Investigation on the influence of different ductile fracture parameters χ for analysis conditions", *Annual Meeting of the Architectural Institute of Japan*, Okayama, Japan.
- Mander, T., Rodgers, G., Chase, J., Mander, J.B., Macrae, G. and Dhakal, R. (2009), "A damage avoidance design steel beam-column moment connection using high-force-to-volume dissipators", *J. Struct. Eng.*, **135**(11), 1390-1397. [https://doi.org/10.1061/\(ASCE\)ST.1943-541X.0000065](https://doi.org/10.1061/(ASCE)ST.1943-541X.0000065).
- Marriott, D., Pampanin, S. and Palermo, A. (2009), "Quasi-static and pseudo-dynamic testing of unbonded post-tensioned rocking bridge piers with external replaceable dissipators", *Earthq. Eng. Struct. D.*, **38**(3), 331-354. <https://doi.org/10.1002/eqe.857>.
- Morgen, B.G. and Kurama, Y.C. (2007), "Seismic design of friction-damped precast concrete frame structures", *J. Struct. Eng.*, **133**(11), 1501-1511. [https://doi.org/10.1061/\(ASCE\)0733-9445\(2007\)133:11\(1501\)](https://doi.org/10.1061/(ASCE)0733-9445(2007)133:11(1501)).
- Nikoukalam, M. and Dolatshahi, K.M. (2015), "Development of structural shear fuse in moment resisting frames", *J. Constr. Steel Res.*, **114**, 349-361. <https://doi.org/10.1016/j.jcsr.2015.08.008>.
- Oktavianus, Y., Goldsworthy, H.M., Gad, E. and Fernando, S. (2019), "The influence of key design parameters on the cyclic axial behavior of innovative replaceable buckling restrained fuses (RBRFs)", *J. Earthq. Eng.*, **23**(7), 1092-1114. <https://doi.org/10.1080/13632469.2017.1351410>.
- Pampanin, S. (2005), "Emerging solutions for high seismic performance of precast/prestressed concrete buildings", *J. Adv. Concr. Technol.*, **3**(2), 207-223. <https://doi.org/10.3151/jact.3.207>.
- Ping, X., Jia, L. J., Ke, K., Chen, Y. and Ge, H.B. (2017), "Ductile cracking simulation of uncracked high strength steel using an energy approach", *J. Constr. Steel Res.*, **138**, 117-130. <https://doi.org/10.1016/j.jcsr.2017.07.002>.
- Sarti, F., Smith, T., Palermo, A., Pampanin, S. and Carradine, D. (2013), "Experimental and analytical study of replaceable buckling-restrained fused-type (BRF) mild steel dissipators", *New Zealand Society for Earthquake Engineering Annual Conference*, Wellington, New Zealand.
- Wada, A., Huang, Y.H. and Iwata, M. (2000), "Passive damping technology for buildings in Japan", *Prog. Struct. Eng. Mat.*, **2**(3), 335-350. [https://doi.org/10.1002/1528-2716\(200007/09\)2:3<335::AID-PSE40>3.0.CO;2-A](https://doi.org/10.1002/1528-2716(200007/09)2:3<335::AID-PSE40>3.0.CO;2-A).
- Wang, C.L., Quan, C., Zeng, B. and Meng, S. (2017), "A novel brace with partial buckling restraint: An experimental and numerical investigation", *Eng. Struct.*, **150**, 190-202. <https://doi.org/10.1016/j.engstruct.2017.06.031>.
- White, S.L. (2014). "Controlled damage rocking systems for accelerated bridge construction", M.S. Thesis; University of Canterbury, Christchurch, New Zealand.
- Xiang, P., Shi, M., Jia, L.J., Wu, M. and Wang, C.L. (2017), "Constitutive model of aluminum under variable-amplitude cyclic loading and its application to buckling-restrained braces", *J. Mater. Civ. Eng.*, **30**(3), 04017304.

[https://doi.org/10.1061/\(ASCE\)MT.1943-5533.0002183](https://doi.org/10.1061/(ASCE)MT.1943-5533.0002183).

Xing, H. (2004), "Research on the mechanical behavior of the parallel thread rebar splicing with rolled thread ends and its application", M.S. Thesis; Dalian University of Technology, Dalian, China. (In Chinese)

Zhou, Z., He, X. T., Wu, J., Wang, C.L. and Meng, S.P. (2014), "Development of a novel self-centering buckling-restrained brace with BFRP composite tendons", *Steel Compos. Struct.*, **16**(5), 491-506. <https://doi.org/10.12989/scs.2014.16.5.491>.

BU